Nanotechnology

PAPER • OPEN ACCESS

Reference-free x-ray fluorescence analysis with a micrometer-sized incident beam

To cite this article: Philipp Hönicke *et al* 2024 *Nanotechnology* **35** 285702

View the article online for updates and enhancements.

You may also like

- Determination of SiO_2 and C layers on a monocrystalline silicon sphere by reference-free x-ray fluorescence analysis
Philipp Hönicke, Ina Holfelder, Michael Kolbe et al.

- A new ^{28}Si single crystal: counting the atoms for the new kilogram definition
G Bartl, P Becker, B Beckhoff et al.

- GRB X-Ray Flare Properties among Different GRB Subclasses
Chuanxi Liu and Jirong Mao

ECS The Electrochemical Society
Advancing solid state & electrochemical science & technology

SUSTAINABLE TECHNOLOGIES

249th
ECS Meeting
May 24-28, 2026
Seattle, WA, US
Washington State
Convention Center

Spotlight
Your Science

Submission deadline:
December 5, 2025

SUBMIT YOUR ABSTRACT

This content was downloaded from IP address 91.181.237.252 on 21/10/2025 at 09:22

OPEN ACCESS
IOP Publishing
Nanotechnology
Nanotechnology **35** (2024) 285702 (8pp)
https://doi.org/10.1088/1361-6528/ad3aff

Reference-free x-ray fluorescence analysis with a micrometer-sized incident beam

Philipp Hönicke[1], André Wählisch[1], Rainer Unterumsberger[1], Burkhard Beckhoff[1], Janusz Bogdanowicz[2], Anne-Laure Charley[2], Hans Mertens[2], Névine Rochat[3], Jean-Michel Hartmann[3] and Narciso Giambacorti[3]

[1] Physikalisch-Technische Bundesanstalt (PTB) Abbestr. 2-12 D-10587 Berlin, Germany
[2] Imec Kapeldreef 75 B-3001 Leuven, Belgium
[3] Univ. Grenoble Alpes CEA, Leti F-38000 Grenoble, France

E-mail: philipp.hoenicke@ptb.de

Received 7 September 2023, revised 19 December 2023
Accepted for publication 5 April 2024
Published 24 April 2024

Abstract
Spatially resolved x-ray fluorescence (XRF) based analysis employing incident beam sizes in the low micrometer range (μXRF) is widely used to study lateral composition changes of various types of microstructured samples. However, up to now the quantitative analysis of such experimental datasets could only be realized employing adequate calibration or reference specimen. In this work, we extent the applicability of the so-called reference-free XRF approach to enable reference-free μXRF analysis. Here, no calibration specimen are needed in order to derive a quantitative and position sensitive composition of the sample of interest. The necessary instrumental steps to realize reference-free μXRF are explained and a validation of ref.-free μXRF against ref.-free standard XRF is performed employing laterally homogeneous samples. Finally, an application example from semiconductor research is shown, where the lateral sample features require the usage of ref.-free μXRF for quantitative analysis.

Keywords: x-ray fluorescence, micro focussed XRF, reference-free analysis, thin-film characterization, nanostructure characterization

1. Introduction

X-ray fluorescence (XRF) analysis with spatial resolution in the micrometer range (micro-XRF or μ-XRF) is a technique that is being widely used to study the elemental composition over a wide range of application fields. Due to the superior features of XRF (nearly no sample preparation, good detection limits, non-destructiveness, easy automation and its measurement capabilities for nearly the full periodic table), it is a highly used technique both at large-scale research facilities and at laboratories using custom build or commercially available tools.

By scanning the sample through the incident micro focussed x-ray beam and detecting the element-specific XRF radiation, elemental maps of a wide range of sample types from liquids [1] to solids and very diverse range of applications including semiconductor research [2], forensics [3], geology [4], biology [5] or archaeometry [6] and archaeology [7] can be acquired. In many cases, however, the required quantitative information on spatial differences in composition needs correction for intricate matrix effects. Raw XRF count rate distributions are not sufficient. To address this issue, there exist fundamental parameter (FP) based physical quantification schemes for μ-XRF [8, 9], similar to those used for standard (non-focussed) XRF applications. However, they require a pre-calibration of the employed instrument using adequate calibration samples—which may be difficult to obtain—as well as good knowledge of the transmission behaviour of the employed micro-focussing optic. In addition, slight changes in the optical beam path, resulting in changes of the transmission behaviour can introduce severe quantification errors.

In this work, a different quantification approach for μ-XRF is demonstrated, which is already well-known from

Original content from this work may be used under the terms of the Creative Commons Attribution 4.0 licence. Any further distribution of this work must maintain attribution to the author(s) and the title of the work, journal citation and DOI.

© 2024 The Author(s). Published by IOP Publishing Ltd

standard XRF [10, 11] and recently also for XRF employing nm-sized incident beams [12]: the so-called reference-free quantification scheme. In contrast to conventional FP-based quantification, it is based on using radiometrically calibrated instrumentation. Thus, all necessary instrumental and geometrical parameters for a quantification are directly available without the need for any calibration sample. As a result, nearly any sample can be directly characterized in a quantitative manner. If the incident photon flux impinging the sample is determined after the incident beam passes through the focussing optic, the transmission function of the optic is not relevant.

We employ a mono-capillary optic in the excitation channel to refocus the monochromatic soft x-ray radiation to spot sizes in the order of 15 μm full-width-at-half-maximum (FWHM). The ref.-free quantification scheme is demonstrated using stratified layer samples for which standard ref.-free XRF can serve as validation in a straightforward manner. Finally, the ref.-free μ-XRF approach is applied to state-of-the-art semiconductor nanostructures. The increased spatial resolution is used to successfully probe the target areas without any background signal from surrounding sample areas. As a result, a recess etch of sacrificial SiGe material within complex nanostructures can be studied.

2. Reference-free x-ray fluorescence analysis

The ref.-free XRF methodology of Physikalisch-Technische Bundesanstalt (PTB) [10, 11] is based on employing physically calibrated and well-characterized instrumentation. This includes well-known excitation sources, for which several well-characterized beamlines are being used at the BESSY II electron storage ring. In the soft x-ray range, the plane-grating monochromator (PGM) beamline [13] for undulator radiation provides x-ray radiation of high spectral purity in the photon energy range from 78 eV to 1860 eV. For the tender- and hard x-ray ranges, both the four-crystal monochromator (FCM) beamline [14] and the BAMline [15] are available for ref.-free XRF experiments. For the monitoring of the incident photon flux as well as for the detection of the emitted XRF radiation, physically calibrated photodiodes [16] and silicon drift detectors (SDD) are being employed. For the latter, not only the photon energy dependent detection efficiencies are being calibrated but also the photon energy dependent detector response [17] is being determined in dedicated experiments employing direct monochromatic synchrotron radiation [18] in special low-electron current shifts at the BESSY II electron storage ring. The detector response functions are important for the reliable deconvolution of the fluorescence spectra especially if fluorescence lines overlap with each other. The detection geometry, which determines the solid angle of detection, is either set by employing a calibrated aperture at a well-known distance with respect to the sample [19] or by a calculation employing the incident beam intensity profile and the relevant SDD detector parameters such as distance and chip aperture area [20, 21]. Finally, the required fundamental parameters (FPs), which quantitatively describe the process of XRF production are taken from databases [22] or from dedicated experiments [23].

The calibrated photon detectors are placed in one of the available in-house-built ultra-high vacuum chambers [19, 24] and then mounted at the respective beamline. This allows the key parameters required for a reference-free quantification of the mass deposition or the areal mass ρd_i of the element i of interest on or within the sample to be determined in a flexible manner. This includes the incident photon flux $\Phi_0(E_0)$ of monochromatic energy E_0 and the effective solid angle of detection Ω. In conjunction with either tabulated or experimentally determined atomic FPs, the following Sherman equation [25] can be used for a quantification of ρd_i:

$$F(\theta_{\text{in}}, E_0) = \frac{\Omega}{4\pi}\frac{1}{\sin\theta_{\text{in}}}\Phi_0(E_0)\epsilon_{E_f}W_i\tau_j(E_0) \times \omega_j T_{i,j} M_{E_0,E_f} \quad (1)$$

with

$$M_{E_0,E_f} = \frac{\left(1 - \exp\left[-\left(\frac{\mu_S(E_0)}{\sin\theta_{\text{in}}} + \frac{\mu_S(E_f)}{\sin\theta_{\text{out}}}\right)\rho d\right]\right)}{\left(\frac{\mu_S(E_0)}{\sin\theta_{\text{in}}} + \frac{\mu_S(E_f)}{\sin\theta_{\text{out}}}\right)}, \quad (2)$$

Here, the recorded count rate for XRF radiation $F(\theta_{\text{in}}, E_0)$ of the element of interest excited employing monochromatic incident radiation of photon energy E_0 and an incident angle θ_{in} is required together with the SDD specific detection efficiency ϵ_{E_f} for the fluorescence line E_f of interest. The relevant atomic FPs such as the photoionization cross section of the respective subshell $\tau_j(E_0)$, the fluorescence yield for that subshell ω_j as well as the transition probability $T_{i,j}$ of the fluorescence line of interest are also required. In combination with sample specific parameters such as the weight fraction W_i of the element within the material of interest and the attenuation correction factor M_{E_0,E_f} (calculated using the sample specific attenuation cross sections μ_S for both incident and XRF photon energies and incident θ_{in} and detection angles θ_{out}, see equation (2)) all relevant parameters required for a quantification are available and the element's mass deposition can be calculated without requiring adequate reference materials or calibration samples.

A sketch of a typical setup for such ref.-free XRF experiments is shown in figure 1 (left). The sample is placed into the center of the respective chamber by means of an x–y scanning stage, and the incident angle θ_{in} between the surface of the sample and the incoming beam is set to 45°. Depending on the beamline employed, the beam size on the sample surface determines the achievable lateral resolution. As all of the excitation volume emits XRF radiation and the employed SDD cannot distinguish between signals originating from different areas within the excitation spot, the beam size is the limiting factor. For the PGM beamline, the FWHM spot size is typically about 40 μm by 220 μm. At the higher-energy beamlines, the spot sizes are usually larger.

If the sample requires a higher lateral resolution, the incident x-ray beam can be refocussed to a smaller spot size employing additional optical elements. For sub-μm lateral resolution, zone-plate based optical setups can be aligned into

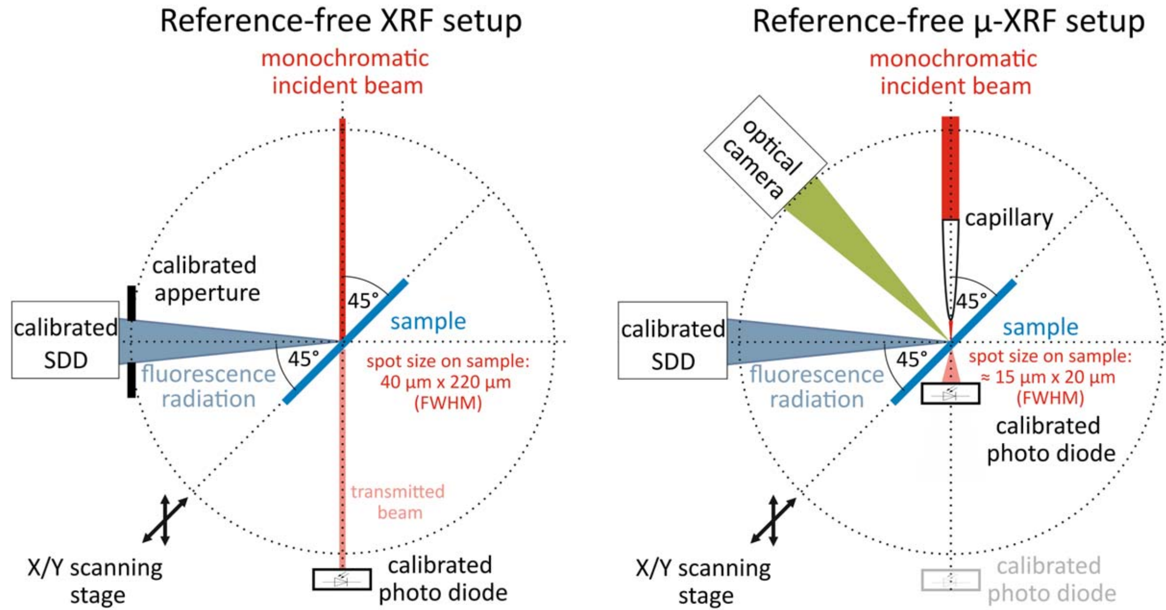

Figure 1. Sketch of the experimental setup for ref.-free XRF and the necessary modifications to enable ref.-free μ-XRF experiments: a focussing optic (here a single-bounce mono-capillary lens is used) is introduced in front of the sample, a calibrated photodiode is mounted on the sample holder and an optical camera for fast beam positioning and optics alignment are mounted into the setup.

the incident beam path [12]. Here, we aim for a lateral resolution in the 10 μm range, for which capillary optics [26] provide excellent intensity amplification in comparison to a classical aperture. In this work, we employ a single-bounce mono-capillary optic as described in another work [27]. This capillary provides a very high transmission, as only one reflection occurs inside the capillary and allows for a realization of spot sizes in the low micrometer range. In figure 1 (right), a sketch of the modified setup for ref.-free μ-XRF experiments is shown. Only minimal modifications are required and spot sizes in the order of 15 μm by 20 μm can be achieved. Depending on the photon energy and the alignment effort, also smaller spot sizes are thinkable but were not required here.

For a successful transfer of the ref.-free quantification principles towards such μ-XRF experiments these modifications to the setup include of course the reshaping of the incident beam. In addition, it must be ensured that the general requirements mentioned earlier are also fulfilled, which is especially crucial for the determination of the incident photon flux. As the photon energy dependent transmission of the capillary lens is often not available at sufficient accuracy and as it is also dependent on the quality of the alignment of the optic with respect to the incident beam, a calculation of the transmitted photon flux is not viable. For an accurate measurement of the transmitted photon flux downstream of the optic, it is crucial to consider the much larger angular divergence of the refocussed x-ray beam as well as its drastically higher photon flux density in the focal point. Due to the latter, it must be ensured that no saturation or destructive effects occur as they would alter the photo diodes linearity and efficiency [28] resulting in erroneous photon flux values. The high divergence of the refocussed beam requires the employed calibrated photo diode to be close enough as it will not be able to detect the full beam if it is positioned too far downstream. As this is the case in the standard setup, the calibrated photodiode is attached to the sample holder for the ref.-free μ-XRF experiments. In contrast to about 40 cm between sample surface and photodiode in the standard setup, this distance is reduced to about 5 cm for the μ-XRF setup. This distance is a good compromise between these two boundary conditions.

For practical reasons, the calibrated aperture defining the solid angle of detection was removed for the ref.-free μ-XRF experiments. This allowed for a realization of larger detection solid angles (by reduction of the sample-detector distance) and thus faster mapping experiments, which was required in order to enable larger area investigations. The solid angle of detection for the ref.-free μ-XRF experiments can then be determined by comparison of detected fluorescence intensities for a given sample with and without the aperture.

3. Experimental

3.1. Beam characterization and photon flux determination

As already mentioned, it is required to determine the incident photon flux for ref.-free μ-XRF experiments. In addition, the characterization of the beam profile with respect to its size in X and Y is also required. The beam profile characterization is important for aligning the capillary optic where both the lateral size as well as the photon flux within the spot are the measurands to be optimized. Secondly, if small sample areas are to be investigated, it must be ensured that the excitation spot is smaller in size than the sample area of interest. If the beam spot would be larger than the lateral distribution of the

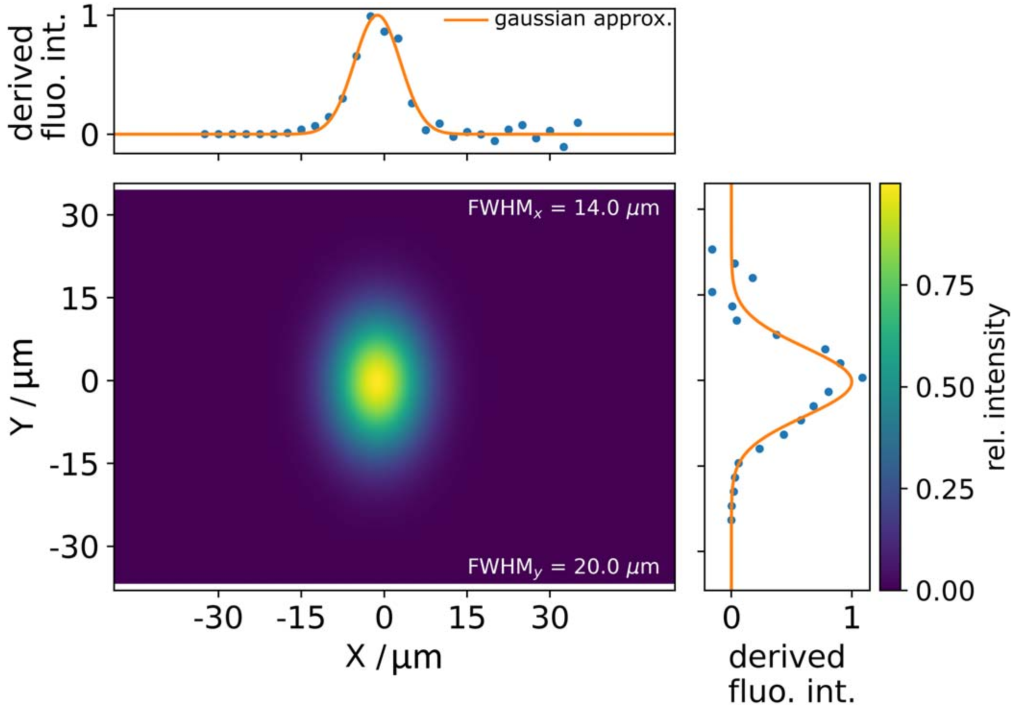

Figure 2. Reconstructed 2D beam profile employing Gaussian approximations of the derived knife-edge scans in X- and Y-direction.

element of interest, the correct areal mass cannot easily be quantified.

The beam spot dimensions can easily be determined employing knife-edge scans in each direction as explained in detail in [27]. The derivatives of the knife-edge scans in X and Y-direction are shown in figure 2. Here it should be noted, that the data quality of the derivative is less good on the side of the knife-edge scan, where the knife-edge starts to cut into the beam. This could be improved by scanning the knife-edge from both sides but was not necessary here. A reconstructed 2D beam profile, based on a 2D Gaussian approximation using the widths of the knife-edge scans in X and Y-direction for the employed capillary is shown in figure 2. As the beam size strongly depends on the alignment of the capillary, this is only a representative result and the beam size must be monitored, for example, when changing the excitation photon energy. For the subsequent experiments, several realignments were performed resulting in slightly different beam size values.

For the determination of the incident photon flux, a 10 mm × 10 mm Si photo diode [29] was mounted much closer to the sample position where also the focus of the capillary optic is aligned to. The diode was mounted in a way that ensures a perpendicular incidence of the incoming photon beam. The detection efficiency of this photo diode can be derived by cross comparison to the calibrated photo diode in the back of the experimental chamber employing the direct x-ray beam. As already mentioned, it must be ensured, that the diode is operated in its linear range even if the photon flux is confined to a small area due to the capillary. This can be checked by comparing the derived photon flux through the capillary to the flux without a capillary in the optical beam path. If this is repeated for several incident flux intensities, the linearity of the diode can be checked.

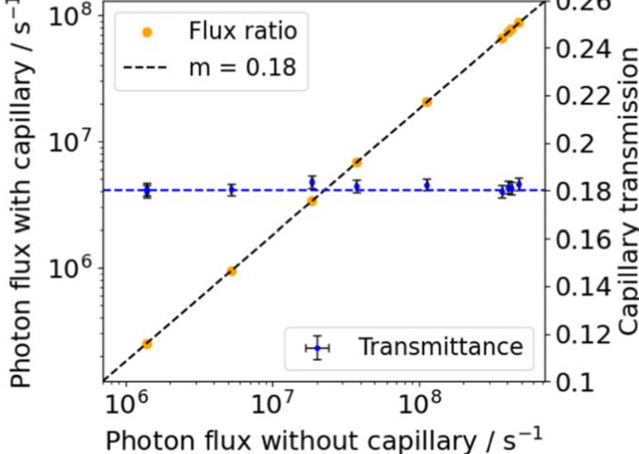

Figure 3. Results of the linearity check of the employed photo diode used for the determination of the incident photon flux for the μ-XRF experiments. For different incident photon fluxes, the ratio of the flux measured using the optic and the flux without the focussing optic was measured. The slope $m = 0.18$ of the black dashed linear fit corresponds to the transmission of the capillary at the employed photon energy of about 1250 eV, which is also shown by the blue data points and the right y-axis. The error bars show the 1-sigma uncertainty of the photon flux, which is mainly determined by the uncertainty of the diode efficiency calibrations.

In figure 3, the outcome of such an experiment is shown. The photon flux available on the sample was varied by changing the exit slit size of the beamline, resulting in a variation of about two orders of magnitude. The straight dashed lines shows that the photo diode is still in its linear

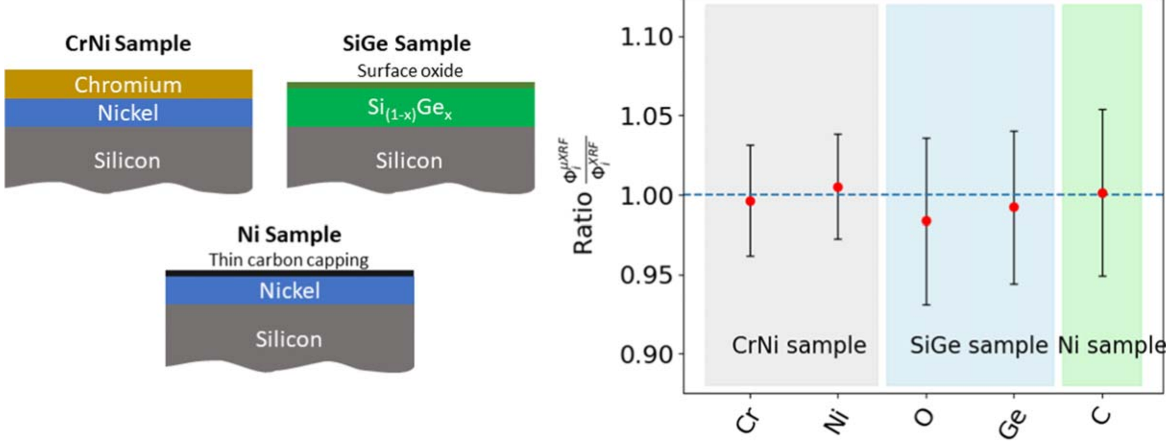

Figure 4. Schematic view of the employed stratified layer samples (left) as well as a comparison of the recorded normalized fluorescence intensities recorded on these samples in standard ref.-free XRF and ref.-free μ-XRF (right). For the Ni sample, only the carbon x-ray fluorescence radiation is used, as the Ni x-ray fluorescence radiation was used for the solid angle determination.

range even if the flux behind the capillary is recorded. The slope of the dashed line is the transmission of the capillary optic for the given alignment, which is also indicated by the blue datapoints.

3.2. Validation of quantification scheme

For both a demonstration and a validation of the proposed scheme for ref.-free μ-XRF experiments, several stratified layer samples were investigated employing 1250 eV as incident photon energy. Their high lateral homogeneity has either been checked in previous studies [19, 30] or are known to fulfill this criterion due to the employed deposition technique. As shown in figure 4, a nanolayer stack of Cr on Ni on silicon wafer (CrNi sample), a silicon-germanium layer also grown on a silicon wafer (SiGe sample) and a nickel nanolayer on silicon (Ni sample). The CrNi and Ni samples have been produced by means of state-of-the-art multilayer optics deposition techniques [31, 32]. The SiGe sample was fabricated at CEA-LETI in a reduced pressure—chemical vapour deposition tool [33]. The SiGe layer with a nominal Ge concentration of 40% was grown at 27 mbar with a SiH_2Cl_2 + GeH_4 chemistry on a 300 mm Si(001) substrate in an Applied Materials Centura 300 epitaxy cluster tool. The growth temperature was set to 600 °C to avoid elastic relaxation for the highest Ge content layer, which would result in a formation of surface undulations. After fabrication, the wafer was measured employing spectroscopic ellipsometry (SE), x-ray diffraction and x-ray reflectometry (XRR), each on multiple spots across the wafer surface.

Again, for a direct comparison of both ref.-free μ-XRF and XRF intensities and quantification results, the lateral homogeneity of the investigated elemental mass deposition must be as good as possible as differently sized irradiated areas are averaged. With the standard ref.-free XRF setup an area of about 0.1 mm^2 is contributing to the overall result whereas only about 0.003 mm^2 contribute employing the μ-XRF setup. Thus, if any inhomogeneities in this range exist, this will result in different XRF signals and eventually different quantification results.

If the lateral homogeneity of the sample is sufficient, the normalized fluorescence intensities of both experimental approaches should be identical if the relevant instrumental parameters for the μ-XRF setup are correctly determined. The normalization is performed as follows:

$$\left[\frac{F}{\Phi_0 \Omega}\right]_{\mu-\mathrm{XRF}} = \left[\frac{F}{\Phi_0 \Omega}\right]_{\mathrm{XRF}}. \quad (3)$$

If the excitation photon energy, the incident and detection angles as well as the employed SDD detector are the same, only the different photon fluxes and solid angles of detection have to be taken into account. As already mentioned, the solid angle defining aperture was removed and thus the solid angle of detection for the μ-XRF experiments was determined using the Ni XRF emission of the Ni-Layer samples. For simplicity and safety reasons, we chose this procedure as for a direct calculation of the solid angle of detection based on the fluorescence detector geometry, its distance to the beam spot on the sample and the incident beam profile as e.g. in [20] one would need to measure the absolute distance between detector and the spot on the sample. Due to the very short distance between the capillary and the sample, this experiment may risk the capillary itself or its alignment. But this issue could relatively easily be circumvented by adding another calibrated aperture at well-known distance closer to the sample if required.

The ratio depicted in equation (3) was calculated for several intense enough XRF lines for the three samples. The results are shown in figure 4 on the right. The uncertainty of this ratio is mainly determined by the counting statistics of the respective fluorescence line, the solid angle calculation as well as the spectral deconvolution. Considering the respective uncertainty, the obtained results agree very well with each other for all samples. Thus, the changes to the setup enable a correct ref.-free quantification also for μ-XRF experiments.

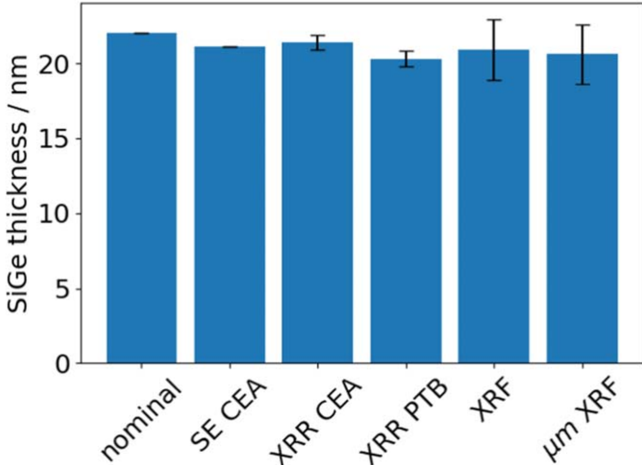

Figure 5. Comparison of the SiGe thickness as quantified by ref.-free μ-XRF in comparison to ref.-free XRF, XRR performed both at PTB and at CEA after fabrication, spectroscopic ellipsometry and the nominal value. It should be noted, that XRR and SE at CEA was performed on multiple points on the full 300 mm wafer and that the presented result is an average value (the standard deviation is depicted as the error bar). For XRR performed at PTB and the two XRF results, the error bars depict the quantification uncertainties.

The SiGe layer thickness was also calculated for the SiGe sample. Here, the XRD derived concentration of Ge (40.37 atomic%) and a corresponding density formula as a function of the Ge concentration [34] was used to derive the layer thickness from the mass deposition. For comparison, also the averaged CEA-LETI results employing SE and XRR, the nominal thickness as well as an additional XRR derived value performed at PTB are provided. The latter was derived by means of a Fourier frequency analysis [35] of reflectometry data measured with an incident photon energy of 1390 eV. As can be seen in figure 5, also the μ-XRF obtained layer thickness agrees very well with the standard XRF result. Both XRF results also agree well with the XRR and SE derived layer thicknesses. It should be noted, that XRR and SE at CEA was performed on multiple points on the full 300 mm wafer and is an average result (the deviation across the wafer is marked as the error bar at CEA XRR data).

3.3. Application example—recess etch monitoring for complex nanostructures

An application which requires the use of μ-XRF is the study of lateral SiGe recess etching in state-of-the-art gate-all-around transistor nanostructures. Here, sacrificial SiGe structures are employed in so-called fork-sheet [36] or nanosheet transistors [37] and must be removed by selective horizontal etching. This is depicted in figure 6(a), where TEM cross sections of the fork-sheet nanostructures are shown for three different recess etch stages (the white material is SiGe). The nominal etch states of the samples A, B and C are no etching (A), medium etch (B) and fully etched (C).

Even though XRF is perfectly suited for such an application as the observable Ge fluorescence signal is a direct monitor for the etch progress [2], it cannot be directly applied due to the size of the homogeneous test patterns available on typical semiconductor dies. Usually, only a very small patch on the die is available for such metrology as shown in figure 6 b. Here, the uniform test pattern has a size of 80 μm^2 and is marked with a white box in panel b. As a consequence, the excitation radiation must be confined to the 80 μm^2 target area as Ge is present also outside the target area in other types of test structures and amounts.

Employing the presented experimental setup for ref.-free μ-XRF, mapping experiments of the target area have been performed for various samples (two of each etching stage). An incident photon energy of 1240 eV was used in order to excite XRF radiation from the L_3-shell of Ge (and not the L_2 shell to avoid Coster–Kronig transitions) as well as the K-shells of oxygen and nitrogen, which are also present within the fork sheet nanostructure. For each position of the sample with respect to the micro-focussed incident beam, spectra were recorded and deconvoluted employing detector response functions [17] for the relevant fluorescence lines as well as background contributions.

The resulting total Ge-L_3 shell—and O–K shell fluorescence intensity distributions obtained on one of the two samples with longest etch duration (C Die 1) are shown in figures 6(c) and (d). The available spatial resolution is sufficient, so that the different square pads within the target area can be identified and that they are well separated from each other to avoid signal cross talk. The slight ripples visible on the outer box are caused by small movements of the incident beam and positioning errors of the employed linear stages. Already these normalized fluorescence signals show, that the various square test pads contain different amounts of material as the four left pads show low Ge signal but high oxygen, whereas the other eight pads have a high Ge and low O signal. The target pad for evaluating the SiGe recess etch can be found in the top row as second pad from the right.

The obtained normalized XRF intensities are averaged within this respective target area (the pad at [0, 0]) to determine a representative result for each sample. Employing equation (1), the present mass deposition of germanium and oxygen can be quantified from the mean values. By using the knowledge on the stoichiometry of the SiGe and the dimensional parameters of the nanostructure, a total thickness of the remaining SiGe layers can be calculated and compared for the six studied samples (two dies of each etch duration were probed). These results are shown in part e of figure 6. The obtained results for the two dies of each etch stage are agreeing very well with each other. But on the nominally fully etched sample C, where no SiGe is supposed to be left in the nanostructure, a small fraction of Ge fluorescence was still detected on both studied dies. This proves that some SiGe is still present. If compared to the unetched sample A, about 3% of the former SiGe amount is remaining. Another study employing secondary ion mass spectrometry at imec found 3.8% of Ge residue on dies from the same wafer [38].

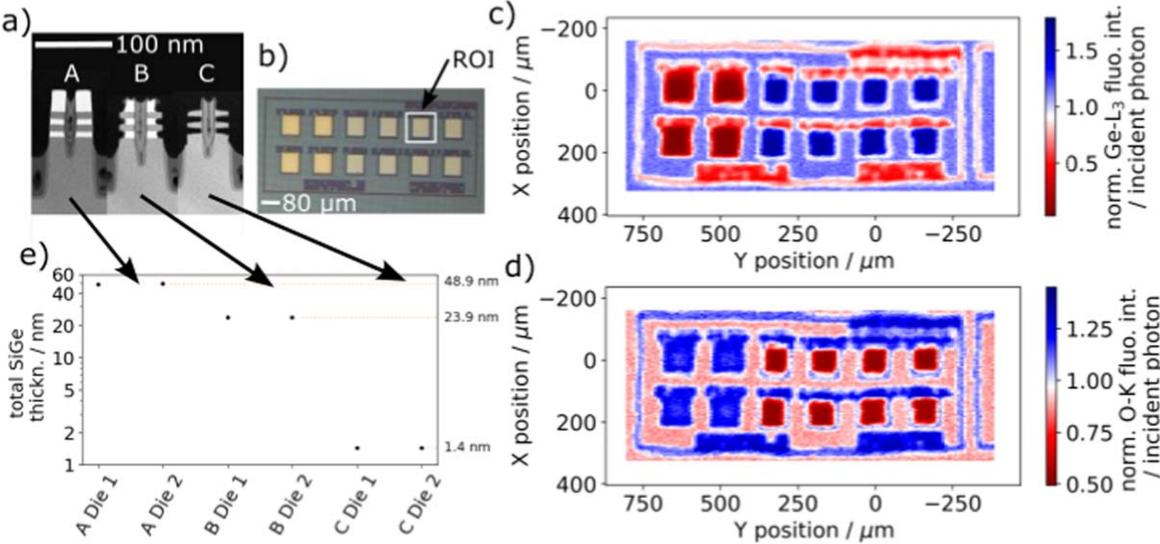

Figure 6. Part (a) shows TEM cross sections of the fork sheet nanostructures at three different etching stages for SiGe removal (bright areas). The homogeneous sample area of interest (ROI) as depicted in the photograph (part b) is only 80 μm^2 in size and marked with a white box. Normalized x-ray fluorescence intensity maps for total Ge-L_3 shell - (part c) and O–K shell fluorescence radiation (part d) of the sample area of interest and surrounding areas for sample C Die 1 are shown. Similar maps where obtained on two dies per etching stage and the Ge areal mass within the ROI area was quantified. The quantification results are shown in part (e). The nominally fully etched sample C, where no SiGe is supposed to be present still contains about 3% of the original SiGe content.

4. Conclusion

In this work, a ref.-free quantification scheme for XRF employing a micrometer-sized excitation beam is demonstrated. Employing capillary-based focussing optics, a small excitation footprint on the sample surface can be realized and employed for lateral mapping of the sample composition. With the application of ref.-free quantification, no standards or calibration specimen are required in order to quantify amounts of material at high spatial resolution. Additionally, the traceability to the SI unit system of the ref.-free approach is retained.

In combination with our earlier works [10, 12], ref.-free XRF is now applicable at multiple spatial resolutions ranging from the mm to the nm range. With this metrological toolset, quantitative composition analysis can be performed at medium to high spatial resolution for a wide range of potential sample systems [39].

Acknowledgments

This project has received funding from the ECSEL Joint Undertaking (JU) IT2 under Grant agreement No. 875999. The JU receives support from the European Union's Horizon 2020 research and innovation programme and the Netherlands, Belgium, Germany, France, Austria, Hungary, the United Kingdom, Romania and Israel. In addition, this project has received funding from the European Union's Horizon 2020 research and innovation programme under Grant agreement No. 861857 CHALLENGES as well as from the Horizon Europe under grant agreement 101096772-14ACMOS.

Data availability statement

Parts of the data cannot be published due to IP issues, but may be made available upon request. The data that support the findings of this study are available upon reasonable request from the authors.

ORCID iDs

Philipp Hönicke https://orcid.org/0000-0002-0712-903X
André Wählisch https://orcid.org/0000-0002-6126-1306
Jean-Michel Hartmann https://orcid.org/0000-0001-7006-8586

References

[1] McIntosh K G, Avery Neal J, Nath P and Havrilla G J 2014 Microfluidic sample preparation for elemental analysis in liquid samples using micro x-ray fluorescence spectrometry *X-Ray Spectrom.* **43** 332–7

[2] Bogdanowicz J, Oniki Y, Kenis K, Puttarame Gowda P, Mertens H, Shamieh B, Leon Y, Wormington M, Van der Meer J and Charley A-L 2023 Model-free measurement of lateral recess in gate-all-around transistors with micro hard-x-ray fluorescence *J. Micro/Nanopatterning Mater. Metrol.* **22** 034001

[3] Nakano K, Nishi C, Otsuki K, Nishiwaki Y and Tsuji K 2011 Depth elemental imaging of forensic samples by confocal micro-XRF method *Anal. Chem.* **83** 3477–83

[4] Flude S, Haschke M and Storey M 2017 Application of benchtop micro-XRF to geological materials *Mineral. Mag.* **81** 923–48

[5] Zhang R, Li L, Sultanbawa Y and Xu Z P 2018 X-ray fluorescence imaging of metals and metalloids in biological systems *Am. J. Nucl. Med. Mol. Imaging* **8** 169–88

[6] Janssens K *et al* 2000 Use of microscopic XRF for non-destructive analysis in art and archaeometry *X-Ray Spectrom.* **29** 73–91

[7] Dumont M, Zoeger N, Streli C, Wobrauschek P, Falkenberg G, Sander P M and Pyzalla A R 2009 Synchrotron XRF analyses of element distribution in fossilized sauropod dinosaur bones *Powder Diffr.* **24** 130–4

[8] Kanngießer B 2003 Quantification procedures in micro x-ray fluorescence analysis *Spectrochim. Acta*B **58** 609–14

[9] Mantouvalou I, Malzer W and Kanngießer B 2012 Quantification for 3D micro x-ray fluorescence *Spectrochim. Acta*B **77** 9–18

[10] Beckhoff B 2008 Reference-free x-ray spectrometry based on metrology using synchrotron radiation *J. Anal. At. Spectrom.* **23** 853

[11] Beckhoff B 2022 Traceable characterization of nanomaterials by x-ray spectrometry using calibrated instrumentation *Nanomaterials* **12** 2255

[12] Wählisch A *et al* 2022 Quantitative element-sensitive analysis of individual nanoobjects *Small* **19** 2204943

[13] Senf F, Flechsig U, Eggenstein F, Gudat W, Klein R, Rabus H and Ulm G 1998 A plane-grating monochromator beamline for the ptb undulators at BESSY II *J. Synchrotron Rad.* **5** 780–2

[14] Krumrey M 1998 Design of a four-crystal monochromator beamline for radiometry at BESSY II *J. Synchrotron Rad.* **5** 6–9

[15] Görner W, Hentschel M P, Müller B R, Riesemeier H, Krumrey M, Ulm G, Diete W, Klein U and Frahm R 2001 BAMline: the first hard x-ray beamline at BESSY II *Nucl. Instrum. Meth.* A **467–468** 703–6

[16] Gottwald A, Kroth U, Krumrey M, Richter M, Scholze F and Ulm G 2006 The PTB high-accuracy spectral responsivity scale in the VUV and x-ray range *Metrologia* **43** 125

[17] Scholze F and Procop M 2009 Modelling the response function of energy dispersive x-ray spectrometers with silicon detectors *X-Ray Spectrom.* **38** 312–21

[18] Beckhoff B, Gottwald A, Klein R, Krumrey M, Müller R, Richter M, Scholze F, Thornagel R and Ulm G 2009 A quarter-century of metrology using synchrotron radiation by PTB in berlin *Phys. Status Solidi*B **246** 1415–34

[19] Kolbe M, Beckhoff B, Krumrey M and Ulm G 2005 Thickness determination for Cu and Ni nanolayers: comparison of reference-free fundamental-parameter based x-ray fluorescence analysis and x-ray reflectometry *Spectrochim. Acta* B **60** 505–10

[20] Beckhoff B, Fliegauf R, Kolbe M, Müller M, Jan Weser and Ulm G 2007 Reference-free total reflection x-ray fluorescence analysis of semiconductor surfaces with synchrotron radiation *Anal. Chem.* **79** 7873–82

[21] Waldschläger P U, Wiesner T, Krämer M and Beckhoff B 2020 Towards a calibration of laboratory setups for grazing incidence and total-reflection x-ray fluorescence analysis *Spectrochim. Acta*B **174** 106009

[22] Schoonjans T, Brunetti A, Golosio B, Sanchez del Rio M, Solé V A, Ferrero C and Vincze L 2011 The xraylib library for x-ray-matter interactions. recent developments *Spectrochim. Acta* B **66** 784

[23] Hönicke P 2023 A novel and holistic approach for experimental x-ray fundamental parameter determination—the Ru L-shell *New J. Phys.* **25** 073012

[24] Lubeck J, Beckhoff B, Fliegauf R, Holfelder I, Hönicke P, Müller M, Pollakowski B, Reinhardt F and Weser J 2013 A novel instrument for quantitative nanoanalytics involving complementary x-ray methodologies *Rev. Sci. Instrum.* **84** 045106

[25] Sherman J 1955 The theoretical derivation of fluorescent x-ray intensities from mixtures *Spectrochim. Acta* **7** 283–306

[26] Bjeoumikhov A, Erko M, Bjeoumikhova S, Erko A, Snigireva I, Snigirev A, Wolff T, Mantouvalou I, Malzer W and Kanngießer B 2008 Capillary μfocus x-ray lenses with parabolic and elliptic profile *Nucl. Instrum. Methods Phys. Res.*A **587** 458–63

[27] Unterumsberger R, Müller M, Beckhoff B, Hönicke P, Pollakowski B and Bjeoumikhova S 2012 Focusing of soft x-ray radiation and characterization of the beam profile enabling x-ray emission spectrometry at nanolayered specimens *Spectrochim. Acta* B **78** 37–41

[28] Sorokin A A, Bican Y, Bonfigt S, Brachmanski M, Braune M, Jastrow U F, Gottwald A, Kaser H, Richter M and Tiedtke K 2019 An x-ray gas monitor for free-electron lasers *J. Synchrotron Radiat.* **26** 1092–100

[29] Sakic A, van Veen G, Kooijman K, Vogelsang P, Scholtes T L M, de Boer W B, Derakhshandeh J, Wien W H A, Milosavljevic S and Nanver L K 2012 High-efficiency silicon photodiode detector for sub-kev electron microscopy *IEEE Trans. Electron Devices* **59** 2707–14

[30] Hönicke P, Krämer M, Lühl L, Andrianov K, Beckhoff B, Dietsch R, Holz T, Kanngiesser B, Weißach D and Wilhein T 2018 Development and characterization of sub-monolayer coatings as novel calibration samples for x-ray spectroscopy *Spectrochim. Acta* B **145** 36–42

[31] Rack A *et al* 2010 Micro-imaging performance of multilayers used as monochromators for coherent hardx-ray synchrotron radiation *Proc. SPIE, 7802* (https://doi.org/10.1117/12.858355)

[32] Krämer M *et al* 2011 Ultrathin layer depositions . a new type of reference samples for high performance xrf analysis *Adv. X-Ray Anal.* **54** 299–304

[33] Hartmann J-M, Mazzocchi V, Pierre F and Barnes J-P 2018 A benchmark of 300 mm RP-CVD chambers for the low temperature epitaxy of si and SiGe *ECS Trans.* **86** 219–31

[34] Levinshtein M E, Rumyantsev S L and Shur M S 2001 *Properties of Advanced Semiconductor Materials: GaN, AIN, InN, BN* (Wiley)

[35] Wernecke J, Shard A G and Krumrey M 2014 Traceable thickness determination of organic nanolayers by x-ray reflectometry *Surf. Interface Anal.* **46** 911–4

[36] Weckx P *et al* 2019 Novel forksheet device architecture as ultimate logic scaling device towards 2 nm *2019 IEEE International Electron Devices Meeting (IEDM)* 36.5.1–.4

[37] Veloso A, Huynh-Bao T, Matagne P, Jang D, Eneman G, Horiguchi N and Ryckaert J 2020 Nanowire and nanosheet fets for ultra-scaled, high-density logic and memory applications *Solid-State Electron.* **168** 107736

[38] Franquet A and Spampinato V unpublished

[39] Hönicke P *et al* 2023 Small target compatible dimensional and analytical metrology for semiconductor nanostructures using x-ray fluorescence techniques *Metrology, Inspection, and Process Control XXXVII* Proceedings Volume 12496 124961J